

RESEARCH ARTICLE

Depth-Resolved and Depth-Integrated Primary Productivity Estimates From In-Situ and Satellite Data in the Global Ocean

HARISH KUMAR KASHTAN SUNDARARAMAN¹ AND PALANISAMY SHANMUGAM¹

Ocean Optics and Imaging Laboratory, Department of Ocean Engineering, Indian Institute of Technology Madras, Chennai 600036, India

Corresponding author: Palanisamy Shanmugam (pshanmugam@iitm.ac.in)

This work was supported by the Ministry of Human Resources and Development (MHRD) and National Geospatial Programme (NGP) of the Department of Science and Technology of Government of India under Grant OEC1819150DSTXPSHA.

ABSTRACT Estimates of marine phytoplankton primary productivity (PP) from satellite remote sensing observations are potentially used to assess global carbon budgets, biogeochemical response, pools and fluxes of carbon and its spatial and temporal variations due to ocean-atmospheric oscillations under climate change. According to the recent studies, satellite-based vertically integrated global PP products have significant uncertainties due to the limitations of the past models, challenges in deriving the appropriate parameters that account for the variation of PP with seasons and provinces, and specify the vertical structure of phytoplankton biomass from satellite observation data and scarcity of in-situ vertical profile data. To overcome these issues, we developed a depth-resolved and depth-integrated model to estimate PP for global oceanic waters. It comprises the depth-resolved primary productivity (DRPP) and satellite-based depth-integrated primary productivity (DIPP) parameterizations to accurately estimate the magnitude and variability of PP in the global ocean. These parameterization algorithms require knowledge of the relative chlorophyll-specific carbon fixation rate (P_{rel}^b) and maximum chlorophyll-specific carbon fixation rate within the water-column (P_{opt}^b) in order to derive the spatial and temporal patterns of DRPP and DIPP. To estimate the chlorophyll-specific maximum rate of carbon fixation at a depth equal to z (P_z^b), two different P_{rel}^b algorithms were developed based on the relative values of i) the subsurface photosynthetically available radiation (PAR_{rel}) and ii) the optical depth at depth z (ζ_z). Furthermore, a sensitivity analysis was conducted to understand the effect of sea-surface temperature (SST), sea-surface chlorophyll concentration (SCHL) and sea-surface photosynthetically available radiation (SPAR) on the photo-physiological parameter (P_{opt}^b). These physical, biological and optical parameters were used to obtain accurate P_{opt}^b estimates. The model based on the SST-SCHL-SPAR (P_{opt}^b (SSTCP)) produced more accurate P_{opt}^b estimates than the global Vertically Generalised Productivity Model (P_{opt}^b (VGPM)). Comparison of the model results with in-situ measurement data demonstrated that the ζ_z -based DRPP algorithm ($DRPP(\zeta_z)$) yields more accurate results than the PAR_{rel} -based DRPP algorithm ($DRPP(PAR_{rel})$). This study also investigates the spatial and temporal patterns in MODIS-Aqua-derived P_{opt}^b and DIPP products and the impacts of climate-driven perturbations on the global ocean PP due to the La Niña and El Niño phenomenon during 2010 and 2015.

INDEX TERMS Primary productivity (PP), maximum carbon fixation rate, depth-resolved PP, depth-integrated PP, ocean color remote sensing, global ocean.

I. INTRODUCTION

Photoautotrophs (phytoplankton: photosynthetic bacteria, diatoms, dinoflagellates, prymnesiophytes, chrysophytes,

The associate editor coordinating the review of this manuscript and approving it for publication was Gerardo Di Martino¹.

and among other organisms) are critical organisms that support the marine environment by providing food (organic matter) to sea creatures and transferring energy through the base-high levels in the marine food chain. These marine organisms are essentially utilizing photosynthetically active radiation (PAR, which designates the range of solar radiation

from 400 - 700 nm) and become responsible for the carbon fixation of 46% (~104.9 petagrams of carbon/year) in the marine environment, which is approximately half of the global productivity [1], [2]. Phytoplankton plays a key role in the ocean ecosystem and contributes approximately 95% of global marine primary production. The factors including light, temperature, nutrients, soil and water affect PP generated by terrestrial plants, whereas light and nutrients are the key environmental factors which affect the marine primary producers [3]. Phytoplanktons utilize inorganic constituents (such as nitrate and phosphate) through the process of photosynthesis and excrete organic compounds (such as lipids and proteins), which have broad implications for the organic carbon fluxes in marine food webs. According to Parsons et al. (1984), the general expression of PP is given by



The photoautotrophs are the main primary producers that use PAR photons to convert inorganic carbon (carbon dioxide (CO₂), bicarbonate (HCO₃⁻), and carbonate (CO₃²⁻)) into organic carbon substances [2], [5]. The rate of production of organic matter per unit area during photosynthesis is referred to as Gross Primary Productivity (GPP), which is usually higher in the sunlit surface ocean layer and decreases with the depth in the ocean where the light intensity is 1% of the sunlight entering the ocean surface. The Net Primary Productivity (NPP, expressed as mg C m⁻² d⁻¹ or g C m⁻² year⁻¹) is the rate of net accumulation of organic materials in the form of biomass, which is obtained by subtracting the autotrophic respiration and other loss terms from the GPP [6], [7].

Marine PP can be estimated from direct and indirect methods (measurements and modelling). For example, Eppley, Nielsen, and Slawyk et al. estimated NPP by using the CO₂ fixation method (¹⁴C and ¹³C assimilation) [8], [9], [10], Dugdale and Goering demonstrated the rate of nutrient uptake for best yields (¹⁵NO₃ and ¹⁵NH₄ assimilation) [11], Williams and Robertson and Williams et al. utilised O₂ evolution from the water (effected by phytoplankton photosynthesis) [12], [13], and Kolber and Falkowski and Kolber et al. used the molecular luminescence (Fluorescence) method where the light energy is captured by electrons circling an atom and a molecule [14], [15]. The most popular methods rely on the light-dependent changes in dissolved oxygen and inorganic carbon to estimate marine PP. For example, the light-dark bottle oxygen method was explored for estimating PP. Later, the carbon-based methods, which use the radioactive isotopic ¹⁴C and ¹³C tracers, were used to estimate marine PP [10], [16]. However, the conventional in-situ measurements provide a lesser spatiotemporal extent and become inadequate for studying the dynamic nature of PP in the global ocean. These methods always require water samples to perform the carbon/oxygen (¹⁴C, ¹³C and ¹⁸O) incubation procedures. During the process of incubation, photosynthesis and the irradiance are measured

and the photosynthesis versus irradiance (P versus E) curves are generated for characterizing phytoplankton physiological responses to environment conditions [17]. Traditional in-situ sampling methods provided a limited number of measurement data which are inadequate for capturing seasonal, inter-annual and multi-decadal variability in PP and its dynamics patterns in regional and global oceanic waters. Moreover, these methods are exhaustive, expensive and time-consuming in the harsh marine environments [18].

Satellite ocean colour (OC) remote sensing provides an important avenue for estimating marine PP and the related physico-chemical and optical properties on regional and global scales. In this context, the first ocean colour satellite sensor named Coastal Zone Color Scanner (CZCS) aboard Nimbus-7 satellite provided time-series data for a large number of locations on the global ocean during 1978 to 1986 and allowed us to estimate phytoplankton pigment abundance for a variety of qualitative and quantitative studies [19], [20]. The CZCS mission made a revolutionary change leading to the development of many OC satellite missions over the past 35 years, namely, Sea-viewing Wide Field-of-view Sensor (SeaWiFS), Moderate Resolution Imaging Spectroradiometer (MODIS), Ocean Colour Monitor (OCM), Medium Resolution Imaging Spectrometer (MERIS), Hyperspectral Imager for the Coastal Ocean (HICO), Geostationary Ocean Color Imager (GOCI), Visible Infrared Imaging Radiometer Suite (VIIRS), Multi-Spectral Instrument (MSI), Ocean and Land Colour Instrument (OLCI) [21], [22].

In the past decades, numerous OC remote sensing algorithms have been developed, tested and validated using satellite-measured water-leaving radiance or remote-sensing reflectance data [23]. For brevity, the satellite-based NPP models are grouped under i) wavelength-resolved models (WRM), ii) wavelength-integrated models (WIM), iii) time-integrated models (TIM), iv) depth-integrated models (DIM), and v) depth-resolved models (DRM) [24], [25], [26], [27], [28], [29], [30], [31]. These models are classified based on the complexity and integration level with wavelength, time and depth. According to the input parameters, the satellite-based NPP models are classified as: i) chlorophyll-based models, ii) carbon-based models, and iii) phytoplankton absorption-based models [32], [33].

In earlier studies, the PP products were derived from the inputs of satellite data products (CZCS, MODIS-Terra/Aqua and GOCI) such as chlorophyll concentration, optimal carbon fixation rate, sea-surface temperature (SST), surface light intensity (PAR) and surface light diffuse attenuation coefficient with certain assumptions and specific relationships among the photosynthetic and physico-chemical parameters [34], [35]. Considerable efforts were also made to estimate PP from MERIS and HICO for inland (lake and lagoon) and near-shore coastal waters [36], [37].

Recently, the primary productivity algorithm round robin (PPARR: 1-3) was conducted to test and evaluate the various NPP models [38]. From the PPARR comparison results, the vertically generalized productivity model

(VGPM) is chosen for this study because of its popularity for processing MODIS-Aqua data for global ocean applications and its advantage of using the readily available satellite-derived products [18], [27], [39]. In general, the accuracy of the satellite-based DIPP estimates may vary depending on the hydrographic conditions and distributions, geographic features, regional characteristics, atmosphere-ocean oscillations under extreme weather events and climate change impacts [40], [41]. One can also estimate a potential change in DRPP and DIPP from the physiological parameter (i.e., the photo adaptive variable, P_{opt}^b).

However, the phytoplankton photo-physiological parameter is difficult to directly derive from satellite remote sensing data. This is because it does not have a direct relationship with the water-leaving radiance or remote-sensing reflectance. Also, there is little data and information on the characteristics of this parameter. Consequently, the existing P_{opt}^b (VGPM) model is less accurate in capturing the environmental condition and variability because of the higher-order function of SST. Few studies have investigated the relationships of PAR and phytoplankton photosynthetic parameter as well as PAR and temperature-based DRPP and DIPP models [42], [43], [44]. According to the previous studies, the above models generally underestimated PP in low-latitude waters and overestimated in mid-latitude waters. At present, there is a challenge in estimating PP at depth 'z' (depth-specific) because of the requirement to specify the vertical structure in phytoplankton biomass, light and photo-physiological parameter (as discussed in Section IV-A and B) [40], [45], [46].

These challenges can be overcome by establishing new empirical relationships among the optically measurable parameters (such as biomass, light, nutrients and temperature) to estimate global DRPP and DIPP and analyze their variations on seasonal, inter-annual and multi-decadal scales. This requires the improved models to estimate DRPP and DIPP in the global ocean. The improved products are necessary for better understanding the biologically-driven and biogeochemical processes associated with the production, sinking and demineralization of organic carbon in the global ocean.

The present work focuses on the depth-resolved and depth-integrated primary productivity estimates from in-situ and satellite data in the global ocean. This is achieved by i) deriving and assigning the appropriate model parameters that link phytoplankton photosynthetic responses to the light field, ii) accounting for their variations with seasons and provinces, and iii) specifying the vertical structure in phytoplankton biomass because satellites observe the ocean surface. In particular, this work is mainly dedicated to

- i) Empirically derive P_{rel}^b models using PAR_{rel} and ζ_z ,
- ii) Assess the performance of our DRPP (PAR_{rel}) and DRPP (ζ_z) models using in-situ PP data,
- iii) Analyze the influence of SST, SCHL and SPAR on the P_{opt}^b estimates,

- iv) Derive new P_{opt}^b models, and
- v) Demonstrate the annual and seasonal variations in P_{opt}^b and DIPP from MODIS-Aqua data using the VGPM and SSTCP models.

II. DATA

A. IN-SITU DATA

For this study, the field measured and globally acquired PP data were obtained from the two different sources of oceanic ^{14}C -database: i) Oregon State University Primary Productivity database (OSPP) (<http://sites.science.oregonstate.edu/ocean.productivity/field.data.c14.online.php>) and ii) Biological and Chemical Oceanography-Data Management Office Primary Productivity database (BCO-DMOPP) (<https://www.bco-dmo.org/dataset/814803>). The summary of the ^{14}C -primary productivity data is given in Table 1.

The OSPP database contains merged data collected on the multiple research cruise programs in different oceanic waters (bounded by latitudes and longitudes of 80.50°N to 76.00°S and 176.40°E to 188.00°W) over the period of 3.5 decades from 1958 to 1994. This provides quality-controlled and in-situ measured ^{14}C -primary productivity data from different oceanic regimes and geographical coordinates. It consists of 3304 vertical profiles of PP and other important parameters such as chlorophyll concentration (Chl), photosynthetically available radiation (PAR), optical depth (ζ), chlorophyll-specific carbon fixation (P^b), maximum chlorophyll-specific carbon fixation (P_{opt}^b), sea-surface temperature (SST) and daylength (DL). The OSPP vertical profiles were previously used for model development (e.g., empirical, machine learning, and artificial neural network approaches) and validation purposes.

A program of the U.S. Joint Global Ocean Flux Study (U.S. JGOFS) and Ocean Carbon and Biogeochemistry (OCB) created the BCO-DMOPP database, which covers global waters bounded by latitudes and longitudes of 60.00°N to 78.00°S and 176.98°E to 178.03°W. The BCO-DMOPP database contains a total of 148 in-situ measured depth profiles of ^{14}C -productivity and related parameters including PAR, chlorophyll pigments (Chl-a/b, carotene, neoxanthin), phytoplankton absorption (a_{ph}), mixed layer depth (MLD) and nutrient measurements (NO_3 , NO_4 , PO_4 , SiO_4 , and NH_4) for the period from 1985 to 2008 (more than two decades of data). Here, the OSPP and BCO-DMOPP data were used after eliminating few vertical profiles due to the missing data/absence of the one or more required parameters (PP, Chl, PAR, SST, P^b , P_{opt}^b , and ζ). The data screening resulted a total of 1340 (out of 3452) vertical profiles of required data (Fig. 1). These data were randomly divided into two datasets: i) one dataset is used for deriving the model parameterizations and it consists of around 55% productivity and other data (the number of vertical profile measurements, $N_p=712$) and ii) one dataset is used for validating the P_{rel}^b and P_{opt}^b products (important inputs for the DRPP and DIPP algorithms) and it consists of around 45% data ($N_p=628$).

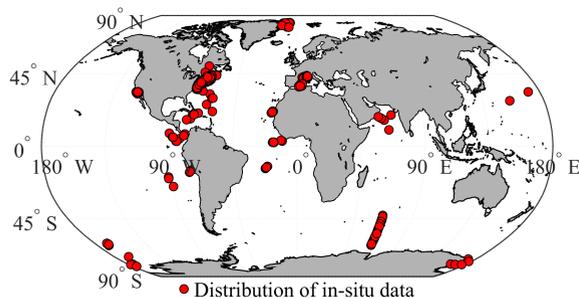


FIGURE 1. A global map showing the geographical locations of in-situ measured primary productivity profiles obtained from the databases of OSPP and BCO-DMOPP (Number of vertical profile measurements, $N_p=1340$).

B. SATELLITE DATA

The Standard Mapped Image (SMI) products were downloaded from the National Aeronautics and Space Administration (NASA)–Ocean Colour Web (<https://oceancolor.gsfc.nasa.gov/13/>) as maintained by the Ocean Biology Processing Group (OBPG), Goddard Space Flight Center. These products were constructed from the Level-3 (L3) binned sensor Moderate Resolution Imaging Spectroradiometer (MODIS)–Aqua images with a spatial resolution of 4 km. For this study, the reprocessed SMI data including SST, SCHL and SPAR (from the MODIS-Aqua sensor) were used to generate the global products of P_{opt}^b and DIPP. To evaluate the model performance in different geographic locations and periods, the present and existing models were applied to SMI data to generate spatial and temporal products of P_{opt}^b and DIPP for the global ocean. In particular, the seasonal images were generated for i) winter: 21 December 2019 – 20 March 2020; ii) spring: 21 March – 20 June 2020; iii) summer: 21 June – 20 September 2020; iv) autumn: 21 September – 20 December 2020; and v) annual: the calendar year of 2020. For this purpose, the MODIS-Aqua images of SST, SCHL and SPAR were obtained and processed using MATLAB codes (R2021b) to generate the global products of P_{opt}^b and DIPP (using the P_{opt}^b (VGPM) and P_{opt}^b (SSTCP)) for the year 2020. In addition, the MODIS-Aqua images of SST, SCHL and SPAR were used to demonstrate the variations in DIPP during the La Niña and El Niño events in 2010 and 2015.

1) VALIDATION AND LIMITATIONS OF THE SATELLITE DATA

The OC products are mainly affected by i) significant influence of CDOM and SS on the reflectance signal which can introduce errors in satellite-derived chlorophyll products for Case 2 waters, ii) attenuation due to the atmospheric constituents – (a) absorption by gas molecules (mainly oxygen, ozone and water vapour), (b) scattering and absorption by aerosols, iii) low solar elevation ($>70^\circ$) which can cause the uncertainty in the SPAR and SCHL estimates, and iv) disparities in spatial and temporal resolution of the input parameters can cause the uncertainty in the OC products. To reduce the uncertainty in the satellite-derived products and improve the quality and consistency of OC products, the NASA-OBPG

performed frequent reprocessing (the recent reprocessing of MODIS-Aqua products was done in July 2022) and produced the “MODIS/Aqua Ocean Colour Reprocessing 2022.0”. This system incorporates the new source files for ancillary data, improved algorithms and updated instrument/vicarious calibration files for the mission.

The NASA-OBPG is responsible for periodical reprocessing of the Ocean Colour (here, SCHL and SPAR) and SST products in order to advance and refine the algorithms and provide additional vicarious calibration data for all supported missions. As a result of the Reprocessing 2022.0, the MODIS-Aqua derived SCHL products were compared with all available in-situ data ($N = 1347$, where ‘ N ’ represents the number of in-situ observations) which were obtained from the Aerosol Robotic Network (AERONET)-OC and SeaWiFS Bio-optical Archive and Storage System (SeaBASS) databases. The statistical analysis between in-situ and satellite-derived SCHL data gave a mean bias of 1.167 mg m^{-3} and a mean absolute error of 1.688 mg m^{-3} [47]. The histogram comparison also showed a close consistency between the satellite-derived SCHL ($0.0211\sim 58.287 \text{ mg m}^{-3}$) and in-situ data ($0.019\sim 58.099 \text{ mg m}^{-3}$). Furthermore, a comparison of the MODIS-Aqua derived SPAR with a limited number of in-situ measurements ($N = 292$) from the COVE site showed a similar mean bias and a mean absolute error of $4.775 \text{ E m}^{-2} \text{ day}^{-1}$ for a range of in-situ (21.745 to $64.438 \text{ E m}^{-2} \text{ day}^{-1}$) and satellite-derived (8.891 to $60.168 \text{ E m}^{-2} \text{ day}^{-1}$) SPAR data [47].

The recent reprocessing of MODIS-Aqua SST was done in December 2019 (denoted as “Reprocessing 2019.0”) and the reprocessed SST were validated with in-situ data for wind speed greater than 6 m s^{-1} . Our analysis showed that the SST gradients in the near-surface layer are affected by the three different processes – subsurface turbulence, heat exchange with the atmosphere and absorption of solar insolation. Under these circumstances, the relationship of sub-surface and skin temperature was found to be nearly stable. The statistical analysis between satellite-derived SST and sub-surface buoy data ($N = 508950$) gave a mean of $-0.185 \text{ }^\circ\text{C}$, a median of $-0.170 \text{ }^\circ\text{C}$, and a standard deviation of $0.423 \text{ }^\circ\text{C}$, whereas a similar analysis between satellite-derived SST and skin radiometer SST data ($N = 2070$) gave a mean of $0.042 \text{ }^\circ\text{C}$, a median of $0.040 \text{ }^\circ\text{C}$, and a standard deviation of $0.494 \text{ }^\circ\text{C}$ [48]. The periodic reprocessing and averaging of OC and SST products over a longer timescale (weekly/monthly) significantly reduced the uncertainties and improved the quality of these products.

III. DESCRIPTION OF THE PP MODELS

The satellite OC models are typically built based on the relationships of phytoplankton biomass (chlorophyll), photosynthetic parameter (PAR) and physical properties (SST) of oceanic water. These models are capable of estimating the ocean PP and its spatial and temporal variations in the near-surface ocean layer on basin and global scales. Given the

depth and surface parameters supplemented by the satellite-based calculations, both DIPP and DRPP are accurately estimated using a set of new models developed in this study (Fig. 2).

A. THE DRPP MODEL

The DRPP model estimates PP at depth ‘z’ by resolving the depth-specific parameters in the water-column. To estimate the depth-specific/resolved PP, a relationship between the chlorophyll-specific carbon fixation rate (P_z^b) and underwater light field measurements at depth ‘z’ was established and included in the DRPP model. This relationship captures the variability of phytoplankton assemblages, but it requires the in-situ measured vertical profiles of i) chlorophyll concentration, ii) chlorophyll-specific photosynthetic rate (P_z^b) and iii) photoperiod. The general form of the depth-resolved (specific) model is given by [31], [49]

$$PP_z = \text{function of } Chl_z, P_z^b \text{ and } DL$$

$$DRPP = PP_z = Chl_z \times P_z^b \times DL \tag{2}$$

where PP_z is primary productivity at depth z, Chl_z is the chlorophyll concentration at depth z, P_z^b is the chlorophyll-specific carbon fixation rate at depth z, and DL represents the photoperiod. The characteristics of the input parameters of the model are described in Table 2. The relative chlorophyll-specific carbon fixation rate within the water-column (P_{rel}^b) is estimated as a function of the chlorophyll-specific carbon fixation rate at depth ‘z’ (P_z^b) and maximum chlorophyll-specific carbon fixation rate within the water-column (P_{opt}^b). To estimate PP accurately, P_z^b is the product of P_{rel}^b and P_{opt}^b and expressed as

$$P_{rel}^b = \frac{P_z^b}{P_{opt}^b}$$

$$P_z^b = P_{rel}^b \times P_{opt}^b \tag{3}$$

Our analysis based on the high-sensitivity in-situ measured ^{14}C -primary productivity profile data showed that P_{rel}^b can be derived from underwater light field data, which include the relative values of the subsurface photosynthetically available radiation (PAR_{rel}) and optical depth (ζ_z). This allows an accurate estimation of PP through the P_{rel}^b and P_{opt}^b models.

B. THE DIPP MODEL

Behrenfeld and Falkowski developed a chlorophyll-based VGPM to estimate NPP [31], [42]. This model is suitable for estimating DIPP on regional and global scales, because it uses the available remote sensing data products as the input parameters (such as SST, SCHL and SPAR).

$$DIPP (VGPM) = SCHL \times P_{opt}^b (VGPM) \times Daylength$$

$$\times 0.66125 \times \frac{SPAR}{SPAR + 4.1} \times Z_{eu} \tag{4}$$

According to Morel and Berthon, the euphotic depth (Z_{eu}) was estimated using the integrated chlorophyll concentration

as a function of SCHL and the term $\left(0.66125 \times \frac{SPAR}{SPAR+4.1}\right)$ represents the irradiance function, which describes the relative change in the light saturation fraction of Z_{eu} and $P_{opt}^b (VGPM)$. The $P_{opt}^b (VGPM)$ model (hereafter, M1) estimates the photo-adaptive parameter using a 7th order polynomial equation with the input of SST and provides the median values of $P_{opt}^b (VGPM)$ for every 1 °C interval increment in SST from -1 to 29 °C. Due to the higher-order function of SST, the VGPM model is not capable of fully capturing the prevailing environmental condition and its variability. The $P_{opt}^b (VGPM)$ is defined as

$$P_{opt}^b (VGPM)$$

$$= 1.2956 + \left(2.749 \times 10^{-1} \times SST\right)$$

$$+ \left(6.17 \times 10^{-2} \times SST^2\right) - \left(2.05 \times 10^{-2} \times SST^3\right)$$

$$+ \left(2.462 \times 10^{-3} \times SST^4\right) - \left(1.348 \times 10^{-4} \times SST^5\right)$$

$$+ \left(3.4132 \times 10^{-6} \times SST^6\right) - \left(3.27 \times 10^{-8} \times SST^7\right) \tag{5}$$

The above formulation is valid for the range of SST 1°C < SST < 28.5°C. If SST < -1°C, the coefficient is set as 1.13 mgC (mg.chl)⁻¹ hr⁻¹. For SST > 28.5°C, it is set as 4.00 mgC (mg.chl)⁻¹ hr⁻¹. At present, the $P_{opt}^b (VGPM)$ products are biased with a large error. To reduce this error, critical environmental and biological parameters for P_{opt}^b are incorporated in the new model that adequately captures the environmental and biological effects [42], [51] and overcomes the deficiency of the models based on a single parameter.

The MATLAB R2021b function was used to implement the DIPP algorithm to estimate $P_{opt}^b (VGPM)$ and $P_{opt}^b (SSTCP)$. The daylength calculation file was obtained from the Math-Works file exchange repository to compute the daylight length for a given year and latitude [52].

IV. DERIVING THE MODEL INPUT PARAMETERS

A. THE P_{rel}^b USING PAR_{rel} DATA

The P_{rel}^b can be accurately estimated by using the depth-wise variation of PP along with Chl_z , subsurface light field and PP_z . Since P_{rel}^b is affected by the light-limited and photo-inhibited parameters, the relationship of P_{rel}^b and PAR_{rel} is necessary in the underwater light field perspective. The vertical profiles of P_{rel}^b and PAR_{rel} measurements are needed to accurately estimate P_z^b . The P_{rel}^b is estimated from in-situ PAR_{rel} data which requires the parameters PAR_z and PAR_{max} .

$$P_{rel}^b = \text{function of } PAR_{rel}$$

$$PAR_{rel} = \frac{PAR_z}{PAR_{opt}} = \frac{PAR_z}{PAR_{max}} = \frac{PAR_z}{PAR_0} \tag{6}$$

The amount of PAR is maximum (PAR_{max}) at the sea-surface and decreases with increase in depth. Here, PAR_{rel} is estimated as the function of the in-situ PAR at depth ‘z’ (PAR_z) to the maximum (optimal) PAR (PAR_{max}). About 55%

TABLE 1. Details of the in-situ ¹⁴C-primary productivity data used for model development and validation purposes.

S.no.*	Region	Cruise program	Period
1	Greenland Shelf (<i>Np</i> =29) North-West Atlantic (<i>Np</i> =173)	NEWP Albatros, Argus, Atlantis, Delaware, Eastward, Gyre, Henlopen, Islin, Kelez76, Kelez77, Knorr77, Knorr80, Mesexi, SEEP	Jul, Aug 1992 Mar, Apr 1975, Mar, Apr, May 1976, Nov, Mar, Aug 1977, Mar, Apr, May, Jun, Jul, Oct 1978, Mar, May 1979, Aug, Sep 1980, Mar 1987, Feb, Jun, Jul, Oct, Nov 1988, Mar 1989, May 1993, Mar, Apr 1994
2	Sargasso Sea (<i>Np</i> =2)	Eumeli	Jun 1992
3	Guinea Dome Zone (<i>Np</i> =4) Mauritanian upwelling (<i>Np</i> =26) North-West Mediterranean (<i>Np</i> =81) Peruvian upwelling/Galapagos (<i>Np</i> =10) Sargasso Sea (<i>Np</i> =7) Sargasso Sea, Gulf of Mexico, tropical eastern Pacific (<i>Np</i> =24) South Indian/Antarctic zone (<i>Np</i> =26) South-West Mediterranean (<i>Np</i> =10)	Guidome Cineca2, Cineca5 Mediproduct Paciproduct Chlomap Discover	Sep, Oct 1976 Mar, Apr 1971, Mar, Apr 1974 Apr 1960, Mar, Apr 1969, Jun, Jul 1972 Sep, Aug 1986 Sep, Oct 1987 May, Jun 1970 Mar 1977 Jun 1990
4	North-West Atlantic (<i>Np</i> =648)	Marmap	Oct, Nov 1978, Feb, Mar, May, Jun, Jul, Aug, Sep, Oct, Nov, Dec, 1979, Feb, Mar, Apr, May, Jun, Jul, Aug, Sep, Oct, Nov, Dec, 1980, Feb, Mar, Apr, Jun, Nov, Dec 1981, Feb, Mar, May, Jun, Nov, Dec 1982
5	California current, Northern Pacific Ocean (<i>Np</i> =270) Gulf stream, Northern Atlantic Ocean (<i>Np</i> =5) Southern Ocean (<i>Np</i> =2)	Cabs5 and 7 Fcr01-22, Fcr25-27 Bbs Martin, Martin-Ross	Sep 1974, Feb, Mar, Jun, Sep, Dec 1975, Mar, Jun, Oct 1976, Jan, Feb, Apr, May, Aug, 1977, Mar, Aug 1978, Mar, Aug 1979, May, Oct 1980, May, Sep, Oct 1981, Mar, Nov 1982, May 1983, Apr 1986, Jan, Apr, Oct 1987 Jan, Feb, Mar, May, Jun, 1960 Jan 1990
6	Arabian Sea (<i>Np</i> =6) Southern Ocean (<i>Np</i> =2)	Ttn-049 Rr-Kiwi-7	Jul, Aug 1995 Dec 1997
7	North Pacific subtropical gyre (<i>Np</i> =1)	Alcyone-iii	Sep 1985
8	Sargasso Sea (<i>Np</i> =3)	Oceanus182-1, 186-2, 192-1	Mar, May, Aug 1987
9	Southern Ocean (<i>Np</i> =2)	Rr-Kiwi-7 and 9	Dec 1997, Mar 1998
10	Southern Ocean (<i>Np</i> =8)	Nbp-97-1	Jan, Feb 1997
11	Boreal North Atlantic (<i>Np</i> =1)	En215	Jul 1990

* 1 - Behrenfeld and Falkowski (Rutgers University), 2 and 3 - Babin and Morel (Laboratoire de Physique et Chimie Marines), 4 - O'Reilly (NOAA, NFMS, Narragansett Laboratory), 5 - Balch (Bigelow Laboratory for Ocean Sciences), 6 - Barber (Duke University), 7 - Bender (University of Rhode Island, URI-GSO), Eppley and Marra (Lamont-Doherty Earth Observatory), 8 - Dickey (University of Southern California) and Marra (Lamont-Doherty Geological Observatory), 9 - Gardner (Texas A&M University) and Barber (Duke University), 10 - Marra (Lamont-Doherty Geological Observatory), 11 - Not available (where *Np* refers the number of vertical profile measurements).

* 1-5 and 6-11 belong to OSPP and BCO-DMOPP databases, respectively.

of the in-situ measured ¹⁴C-PP data (*Np*=712) were used to derive an empirical formulation to estimate P_{rel}^b as the function of PAR_{rel} . It takes the form as

$$P_{rel}^b = \frac{(104.6 \times PAR_{rel} + (-4.003))}{(11.89 + PAR_{rel})} \quad (7)$$

The median values of P_{rel}^b were calculated for each 5 Einstein m⁻² d⁻¹ interval of PAR increment from 0 to 100% of PAR_{rel} (Fig. 3 (a)). The above formulation captures the effect of the underwater light field and estimates P_{rel}^b from the in-situ PAR profile data.

B. THE P_{rel}^b USING ζ_z DATA

It is assumed that the PP_z and light saturation depth vary linearly with PAR given that the light saturated photosynthesis

rate is nearly constant and does not affect the quantum yields of phytoplankton photosynthesis. Earlier studies have concluded that in the absence of photoinhibition in open oceans, the vertical structure of PP will display a region of light saturation in the surface layer and a region of light limitation in the deeper layer. Because most of the in-situ PP profiles were obtained without subsurface PAR measurement data, the vertical attenuation coefficient of PAR (K_{PAR}) is incorporated in the P_{rel}^b model, which is given by

$$P_{rel}^b = \text{function of } \zeta_z$$

$$\zeta_z = K_{PAR} \times z \quad (8)$$

This method is useful when there is the lack of PAR measurements associated with PP profile data. It can be extended

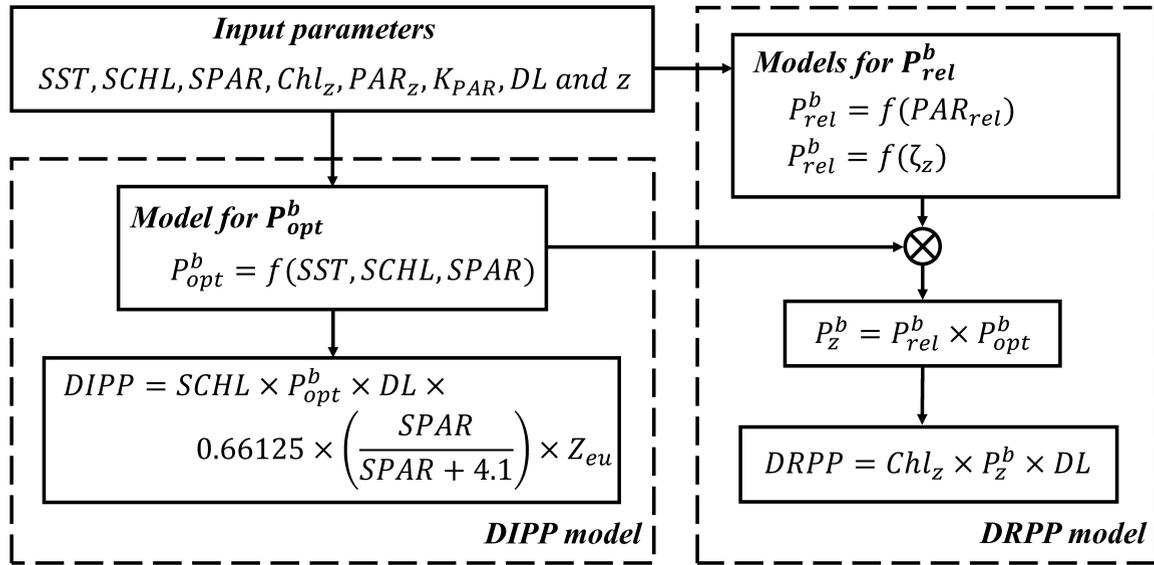


FIGURE 2. A flowchart describing the key-steps involved in the DRPP and DIPP models.

TABLE 2. Description of the parameters and symbols used in this study.

Parameter	Description	Unit/Remark
VGPM	Vertically generalized productivity model (Behrenfeld and Falkowski,1997)	Existing model
SSTCP	Sea-surface temperature, chlorophyll and PAR model	Present study
DRPP/PP _z	Depth-resolved primary productivity / primary productivity at the depth z	mg C m ⁻³ d ⁻¹
DIPP/NPP	Depth-integrated primary productivity / net primary productivity	mg C m ⁻² d ⁻¹
z	Sample (measurement) depth in the water column	m
Chl _z	Chlorophyll concentration at the depth z	mg chl m ⁻³
P _z ^b	Chlorophyll-specific carbon fixation rate at the depth z	mg C (mg chl) ⁻¹ hr ⁻¹
P _{rel} ^b	Relative chlorophyll-specific carbon fixation rate within a water column	unitless
P _{opt} ^b	Maximum chlorophyll-specific carbon fixation rate within a water column	mg C (mg chl) ⁻¹ hr ⁻¹
PAR _{rel}	Relative values of the subsurface photosynthetically available radiation	unitless
PAR _z , PAR _{max} and PAR ₀	Photosynthetically available radiation at the depth z, maximum and surface level respectively	Einstein m ⁻² d ⁻¹
ζ _z	Optical depth values at the depth z	unitless
K _{PAR}	Vertical attenuation coefficient of PAR	m ⁻¹
SCHL	Sea-surface chlorophyll	mg chl m ⁻³
SPAR	Sea-surface photosynthetically available radiation	Einstein m ⁻² d ⁻¹
SST	Sea-surface temperature	°C
DL	Photoperiod	hours
Z _{eu}	Euphotic depth (at a depth where 1% surface PAR reaches)	m
P _{opt} ^b (VGPM)	Maximum chlorophyll-specific carbon fixation rate within a water column derived from VGPM, Behrenfeld and Falkowski (1997)	mg C (mg chl) ⁻¹ hr ⁻¹
P _{opt} ^b (SSTCP)	Maximum chlorophyll-specific carbon fixation rate within a water column derived using SST, SCHL and SPAR	mg C (mg chl) ⁻¹ hr ⁻¹
DIPP(VGPM)	Depth-integrated primary productivity derived from VGPM	mg C m ⁻² d ⁻¹
DIPP(SSTCP)	Depth-integrated primary productivity derived from SSTCP	mg C m ⁻² d ⁻¹

through the depth to describe the photosynthesis-irradiance parameters. The product of physical depth (z) and vertical attenuation coefficient of PAR (K_{PAR}) gives the optical depth (ζ_z) in the water-column (8). Normalizing the physical depth by the optical depth using the appropriate coefficients and parameters gives P_{rel}^b ,

$$P_{rel}^b = 82.39 \times \exp\left(-\left(\frac{\zeta_z - 0.5998}{2.1460}\right)^2\right) \quad (9)$$

The vertical profile of P_{rel}^b can be estimated as a function of the optical depth (not physical depth). About 55% of the in-situ measured ζ_z ($Np=712$) were used to derive the above formulation. Figure 3 (b) shows a relationship between the observed median values of P_{rel}^b and ζ_z (with an increment of 0.2 in the range from 0 to 6, which is a unitless quantity).

C. THE P_{opt}^b USING SST, SCHL AND SPAR

The P_{opt}^b in regional and global oceanic waters was estimated by two different methods: i) using the historically collected

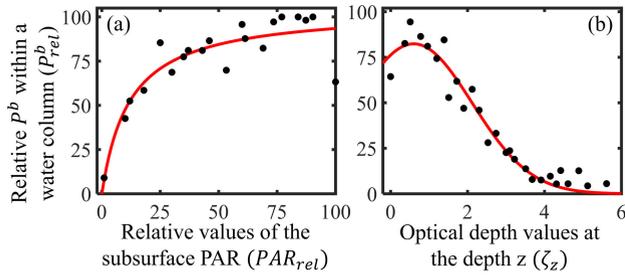


FIGURE 3. A relationship of the relative chlorophyll-specific carbon fixation rate in the water column (P_{rel}^b) established from (a) the relative values of the subsurface photosynthetically available radiation (PAR_{rel}) and (b) the optical depth values at depth z (ζ_z).

photosynthesis-irradiance data for geographically classified oceanic provinces [53] and ii) using an empirical approach that relates the observed P_{opt}^b to the environmental and biological forcing parameters [25], [42]. Depending on the specific application, one of these methods can be chosen as the former approach provides the coarser-scale physiological variability in the region of interest [54] and the later approach gives the phytoplankton biomass variability based on the P_{opt}^b . Earlier studies have focused on the characteristics of the input parameters of the model such as chlorophyll, PAR and P_{opt}^b and proposed better refinements on the estimation of underwater light field [20], [44], [55]. A considerable progress was also made to describe the vertical distribution of chlorophyll [50], [55].

Our study demonstrated that the P_{opt}^b estimates require further improvement based on the critical physical, biological and optical parameters (SST, SCHL and SPAR). These parameters are incorporated into the calculation of P_{opt}^b , because i) SST can be used as a proxy to determine the light and nutrient concentrations at the sea-surface / near-surface waters, which define the photosynthetic capacity of phytoplankton [56], [57], [58], [59], ii) the abundance of phytoplankton is indexed by the chlorophyll concentration in the marine environment. Moreover, PP is affected by the size-fractionated phytoplankton communities. For instance, the small-sized phytoplankton is dominant over the larger-sized phytoplankton in many ocean provinces. The SCHL is a biotic factor and serves as a proxy for phytoplankton biomass.

The photosynthetic efficiency is affected by the size and composition of phytoplankton by changing the photosynthetic light absorption characteristics [60], iii) Generally, there is a significant change in the surface-reaching-irradiance (light availability) at different time scales (day and night, seasonal and annual). Accordingly, the phytoplankton community adopt this change in the light-harvesting capacity and the light-limited and photo-inhibited parameters control the magnitude of P_{opt}^b . Specifically, the photo-inhibited parameter alters the depth of P_{opt}^b in the water-column. The flow of the photochemical energy at different light intensity levels in the phytoplankton cellular structure can be represented by adding the light component in the P_{opt}^b model [42]. The photophysiological characteristics of phytoplankton are

distinct in different light environments, and physical and chemical conditions, which dictate the in-situ growth of phytoplankton over time and across the oceanic provinces. Thus, the SST, SCHL and SPAR can be used to estimate P_{opt}^b in the global ocean.

To estimate the spatial and temporal variability of phytoplankton carbon fixation in global oceanic waters, our model includes the effects of environmental and biological factors on the P_{opt}^b . The physiological nature of phytoplankton mainly depends on the availability of light and nutrients in the water-column. Thus, the association of the environmental and biological forcing parameters with P_{opt}^b was studied for a better representation of the ideal photo-adaptive parameter. In this study, the median values of SCHL, SPAR and P_{opt}^b were calculated from those of SST within the range from -1.3 to 31.8 °C (with 1 °C interval increment). For performance assessment, the resultant data consisting of 32 in-situ measurements (SST, SCHL, SPAR and P_{opt}^b) out of 712 data were used. Our analysis showed a positive correlation of P_{opt}^b with SST and SPAR, and a negative correlation of P_{opt}^b with SCHL in global oceanic waters owing to its causative association with the environmental and biological factors (refer Fig. 4 (a)-(c)). This parameter helps to emphasize photo-acclimation and nutrient-dependence changes in global ocean waters (detailed discussions presented in section VI-A).

In this study, we developed a total of seven P_{opt}^b models (from M2 to M8, further details in Table 3); i) the uni-parameter models (M2 to M4) developed using a single input parameter (e.g., SST, SCHL and SPAR), ii) the bi-parameter models (M5 to M7) developed using a combination of the two input parameters (e.g., SCHL-SPAR, SST-SCHL, and SST-SPAR), and iii) the tri-parameter model (M8) developed using a combination of the three input parameters (e.g., SST-SCHL-SPAR together).

V. PERFORMANCE ASSESSMENT

Performance assessment of the P_{opt}^b , *DIPP* and *DRPP* models was done based on the most common statistical metrics such as mean relative error (MRE), Pearson-correlation coefficient (PCC), mean absolute error (MAE), root mean square error (RMSE) and mean net bias (MNB) [33], [61]. These metrics are defined as

$$\text{MRE(ABS)} = \frac{1}{n} \sum_{i=1}^n \left(\frac{|X_i^{\text{modelled}} - X_i^{\text{in-situ}}|}{X_i^{\text{in-situ}}} \right) \quad (10)$$

$$\text{PCC} = \frac{\sum_{i=1}^n (X_i^{\text{in-situ}} - X_i^{\text{in-situ_mean}})}{\sqrt{\sum_{i=1}^n (X_i^{\text{in-situ}} - X_i^{\text{in-situ_mean}})^2}} \times \frac{(X_i^{\text{modelled}} - X_i^{\text{modelled_mean}})}{\sqrt{\sum_{i=1}^n (X_i^{\text{modelled}} - X_i^{\text{modelled_mean}})^2}} \quad (11)$$

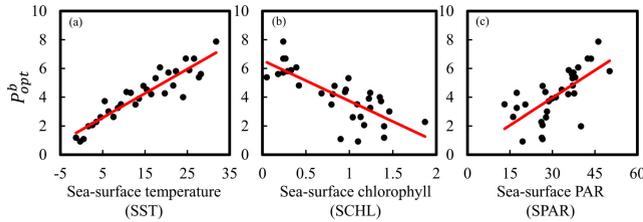


FIGURE 4. Relationships of the maximum chlorophyll-specific carbon fixation rate within the water column (P_{opt}^b) and (a) sea-surface temperature (SST: °C), (b) sea-surface chlorophyll (SCHL: mg.chl m⁻³), and (c) sea-surface photosynthetically available radiation (SPAR: Einstein m⁻² d⁻¹).

$$MAE = \frac{1}{n} \sum_{i=1}^n |X_i^{modelled} - X_i^{in-situ}| \quad (12)$$

$$RMSE = \sqrt{\frac{1}{n} \sum_{i=1}^n (X_i^{modelled} - X_i^{in-situ})^2} \quad (13)$$

$$MNB = \frac{1}{n} \sum_{i=1}^n (X_i^{modelled} - X_i^{in-situ}) \quad (14)$$

where X_i represents the P_{opt}^b , $DRPP (PAR_{rel})$ and $DRPP (\zeta_z)$.

VI. RESULTS AND DISCUSSION

The spatiotemporal variations in P_{opt}^b , DRPP and DIPP are largely caused by the physical (mixing and stratification, thermohaline circulation, mixing of waters, upwelling and downwelling), chemical (nutrient, carbon, oxygen and trace metal cycling, and remineralization) and biological parameters (grazing by zooplankton and biological pumps). These complex processes are controlled by the SST, SCHL and SPAR. In this study, multiple regression equations were developed and validated to capture the variations of these properties in the global ocean. To demonstrate the spatial and magnitude variations of P_{opt}^b , the DIPP formulations of this study were applied to the MODIS-Aqua Level-3 seasonal and annual images.

A. EVALUATION OF THE P_{opt}^b MODELS

This section provides the statistical comparison of uni-, bi- and tri-parameter P_{opt}^b models using independent in-situ data ($N_p=628$) and the scatterplot comparison of all P_{opt}^b models (Fig. 5). Statistical results showed that the $P_{opt}^b (SSTCP)$ (M8) had better performance in terms of the correlation coefficient (PCC: 0.335) and errors (MRE: 0.757; MAE: 1.856; RMSE: 2.440 and MNB: 0.283) than the standard $P_{opt}^b (VGPM)$ (M1) and other models (M2-M7) developed in this study (Table 4). The ranges of these statistical metrics for the M1-M7 models are PCC: 0.165-0.330; MRE(ABS): 0.764-0.978; MAE: 1.867-2.292; RMSE: 2.429-2.878 and MNB: (-0.633)-0.299, which clearly indicate the lower performance of these models as compared to the M8.

To investigate the spatial distribution and temporal variation of P_{opt}^b , the MODIS-Aqua images of the year 2020 were processed and the results shown in Figs. 6 and 7. Note that

TABLE 3. Details of the present models to estimate P_{opt}^b .

Model No.	Newly developed P_{opt}^b models
M2	$P_{opt}^b = 0.1688 \times SST + 1.7340$
M3	$P_{opt}^b = 10^{(-0.2508 \times SCHL + 0.8269)}$
M4	$P_{opt}^b = 0.1106 \times SPAR + 0.8395$
M5	$P_{opt}^b = 10^{(-0.3044 \times SCHL + 0.7088)} + 10^{(0.0210 \times SPAR - 0.6250)}$
M6	$P_{opt}^b = (0.1570 \times SST - 4.0713) + 10^{(-0.0214 \times SCHL + 0.7945)}$
M7	$P_{opt}^b = (0.1560 \times SST + 1.0966) + (0.0197 \times SPAR + 0.2021)$
M8	$P_{opt}^b = (0.1497 \times SST - 3.3061) + (0.0178 \times SPAR - 4.2006) + 10^{(-0.0091 \times SCHL + 0.9598)}$

the M1 underperformed (MRE: 0.978, MAE: 2.046, RMSE: 2.613 and MNB: -0.633) because of its higher order polynomial SST relationship being inadequate to replicate the characteristics of P_{opt}^b . As a result, the M1 produced high values in midlatitude ocean waters and low values in tropical and polar ocean waters (Fig. 6 (d)). The frequency distribution of M1 values is centered at 4 mg C (mg.chl)⁻¹ hr⁻¹, which is due to the fact that the Behrenfeld and Falkowski model assigned the constant P_{opt}^b value (4 mg C (mg.chl)⁻¹ hr⁻¹) for the SST >28.5 °C [31].

In the previous section, significant relationships of P_{opt}^b with SST, SCHL and SPAR (refer Fig. 4) were demonstrated and allowed to develop the multiparameter P_{opt}^b models [uni-parameter models (M2-M4), bi-parameter models (M5-M7) and tri-parameter model (M8)]. The results of these models to capture the biogeochemical variations in the global ocean are shown in Fig. 6 (e)-(g). In general, the uni-parameter models (M2-M4) produced biased P_{opt}^b (global spatiotemporal variability) as the result of the single input parameter, which limits our ability to capture the effects of physical and biological environmental parameters in the marine environment [42]. The bi-parameter models (M5-M7) showed spatial patterns of P_{opt}^b consistent with M8 (Fig. 6 (h)-(k)) with slightly higher errors (Table 4). The overall ranges of the global P_{opt}^b values derived from the M2-M7 are given as follows: mean: 4.154-5.565, median: 4.144-6.017 and standard deviation: 1.262-1.934.

The P_{opt}^b estimates derived from the standard model (M1) and other models developed in this study (M2-M7) are inadequate to represent the effects of light-limitation, photo-saturation and photoinhibition in the global ocean. The frequency distribution of M8 indicates that the P_{opt}^b values are spread throughout the range of 0.000-7.587 mg C (mg.chl)⁻¹ hr⁻¹ (as shown in Fig. 7 (h)). In addition, it exhibits a bimodal distribution with peaks around 2 and 7 mg C (mg.chl)⁻¹ hr⁻¹. The statistical metrics showed small errors and high correlation coefficients for M8, which indicates its higher performance over the M1-M7 models to capture the variability of P_{opt}^b in the diverse marine environments.

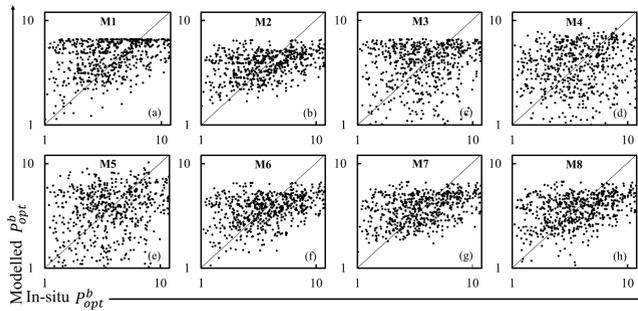


FIGURE 5. Scatterplot comparison between the in-situ measured maximum chlorophyll-specific carbon fixation rate within the water column (P_{opt}^b) and the empirically-derived P_{opt}^b values from (a) VGPM model: M1 (P_{opt}^b (VGPM)), (b-d) uni-parameter models: M2-M4, (e-g) bi-parameter models: M5-M7, and (h) tri-parameter model: M8 (P_{opt}^b (SSTCP)) respectively.

To analyse the seasonal variability in P_{opt}^b , the M1 and M8 models used to process the MODIS-Aqua seasonal images (Fig. 8). In spring and summer, phytoplankton are able to photosynthesize at a faster rate, resulting in a high P_{opt}^b as shown in Fig. 8 (r) and (s). In autumn and winter, phytoplankton growth slows down resulting in a low P_{opt}^b as seen in Fig. 8 (q) and (t).

B. EVALUATION OF THE DRPP MODEL

The DRPP is modelled as the function of Chl_z , DL and P_z^b , as given in (2). The Chl_z and DL are directly / accurately obtained from in-situ measurement data, which can be used in the DRPP models. The modelling of P_z^b is complicated because of the challenge in defining the subsurface light fields and its controlling parameters P_{opt}^b and P_{rel}^b in diverse marine environments. In this study, the M1-M8 models were presented to calculate the P_{opt}^b (detailed discussion given in Section VI-A) and two different approaches were developed to obtain P_{rel}^b : i) one approach the PAR_{rel} data (7), and ii) one approach uses the ζ_z data (9). By substituting the P_{rel}^b (7 and 9) and P_{opt}^b (M1-M8) in (3), we obtained sixteen P_z^b models. By substituting these sixteen P_z^b models in (2), we obtained sixteen DRPP models. For a better representation, these sixteen DRPP models are grouped as i) eight $DRPP(PAR_{rel})$: M1_PAR to M8_PAR, and ii) eight $DRPP(\zeta_z)$: M1_OD to M8_OD. Figure 9 shows the comparisons of these models.

To evaluate the accuracy of these DRPP models, the model results were compared with in-situ vertical profile measurement data (Table 5) ($N_p=628$). It should be mentioned that the $DRPP(\zeta_z)$ -M8_OD yielded a higher accuracy / performance in terms of PCC (0.746) and statistical metrics (MRE: 1.137; MAE: 17.96; RMSE: 37.71 and MNB: 5.134) over the other models.

C. GLOBAL DISTRIBUTION OF DIPP(VGPM) AND DIPP(SSTCP) USING SATELLITE DATA

The global and regional PP levels are generally influenced by seasonal environmental changes, light and nutrients [62].

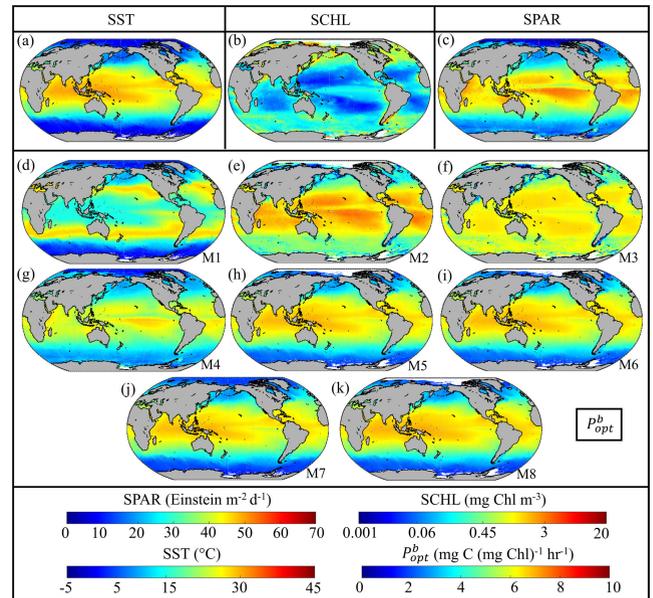


FIGURE 6. (a-c) The annual MODIS-Aqua images of SST, SCHL and SPAR used as the input parameters for the P_{opt}^b and obtained from (d) M1 (P_{opt}^b (VGPM)), (e-g) uni-parameter models: M2-M4, (h-j) bi-parameter models: M5-M7, and (k) tri-parameter model: M8 (P_{opt}^b (SSTCP)) for the year 2020.

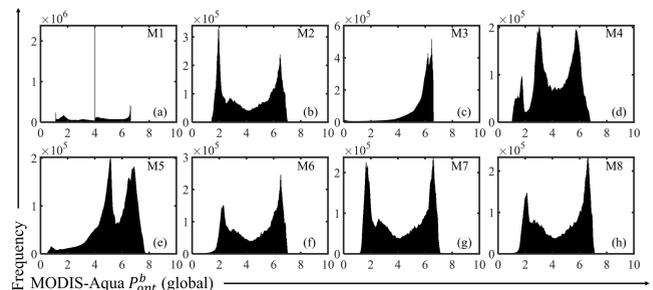


FIGURE 7. Histogram comparison of the maximum chlorophyll-specific carbon fixation rate within the water column (P_{opt}^b) obtained from the global MODIS-Aqua images (as shown in Fig. 6) using (a) VGPM model: M1 (P_{opt}^b (VGPM)), (b-d) uni-parameter models: M2-M4, (e-g) bi-parameter models: M5-M7, (h) tri-parameter model: M8 (P_{opt}^b (SSTCP)) for the year 2020.

The seasonal variability mainly occurs due to the availability of light and nutrients caused by vertical mixing in the water column. To analyse the spatiotemporal variation in the DIPP products, the DIPP models were applied to MODIS-Aqua data for generating the seasonal and annual images for the year 2020. The Behrenfeld and Falkowski [31] model was used to derive the DIPP(VGPM) and DIPP(SSTCP) products from satellite data with the inputs of P_{opt}^b from two different models: i) P_{opt}^b (VGPM) and ii) P_{opt}^b (SSTCP). The DIPP products based on the inputs of Z_{eu} and P_{opt}^b derived from the SST, SCHL and SPAR, and daylength are more accurate in detecting the seasonal and inter-annual variations on a global scale [63].

The polar region exhibits the vertically uniform temperature (diminutive thermocline) and uninterrupted nutrient

TABLE 4. Comparison of the P_{opt}^b models obtained from the VGPM (M1) and the new models (M2-M8) with in-situ P_{opt}^b measurements. (UNIT: $mg\ C\ (mg\ chl)^{-1}\ hr^{-1}$).

Models	M1	M2	M3	M4	M5	M6	M7	M8
	(SST-7 th order)	(SST)	(SCHL)	(SPAR)	(SCHL-SPAR)	(SST-SCHL)	(SST-SPAR)	(SST-SCHL-SPAR)
MRE(ABS)	0.978	0.780	0.930	0.923	0.899	0.764	0.778	0.757
PCC	0.302	0.321	0.178	0.165	0.238	0.330	0.321	0.335
MAE	2.046	1.867	2.292	2.234	2.173	1.873	1.870	1.856
RMSE	2.613	2.429	2.878	2.839	2.789	2.447	2.441	2.440
MNB	-0.633	0.164	0.273	0.031	0.129	0.299	0.193	0.283
Mean of in-situ derived P_{opt}^b (validation)	4.710	3.913	3.804	4.046	3.948	3.778	3.885	3.794
Mean of satellite derived P_{opt}^b (global)	3.969	4.249	5.562	4.150	5.434	4.605	4.216	4.567
Range of in-situ derived P_{opt}^b (validation)	1.130-6.627	1.515-6.528	0.009-6.636	0.987-8.427	0.424-10.276	0.173-6.603	1.407-6.703	0.677-6.731
Range of satellite derived P_{opt}^b (global)	1.106-6.627	1.430-8.483	0.000-6.695	0.840-8.438	0.299-10.265	0.000-7.520	1.088-8.414	0.000-7.587

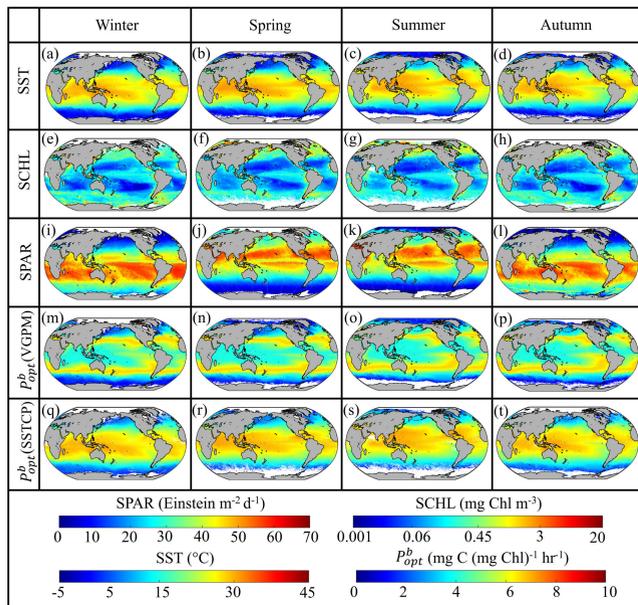


FIGURE 8. The MODIS-Aqua seasonal images of (a-d) SST, (e-h) SCHL and (i-l) SPAR used as the input parameters for the P_{opt}^b obtained from (m-p) VGPM model: M1 (P_{opt}^b (VGPM)), (q-t) tri-parameter model: M8 (P_{opt}^b (SSTCP)) for winter, spring, summer and autumn of 2020.

supply by mixing processes, which confirm that PP in this region is not limited by nutrients. The PAR is low in winter and acts a primary limiting factor, causing the seasonal PP changes in polar oceans. Consequently, PP is lowest in winter despite the abundance and mixing of nutrients in the water-column (Fig. 10 (a) and (b)). The increased levels of nutrients and PAR together cause algal blooms during the spring and summer, resulting the high primary production (Fig. 10 (d-f) and (g-i)). These algal blooms start to decay with the depletion of nutrients and reduction of PAR, resulting the lower primary production during the autumn and winter (Fig. 10 (j-l) and (a-c)).

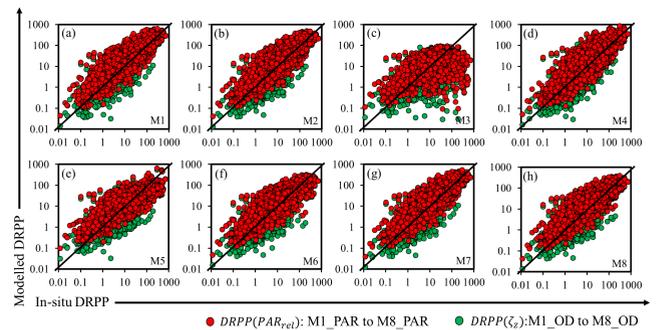


FIGURE 9. Scatterplot comparison of the in-situ measured DRPP values and the empirically modelled DRPP values obtained from i) P_{rel}^b using the PAR_{rel} measurements (red colour filled circle) and ii) P_{rel}^b using the ζ_z measurements (green colour filled circle) for (a-h) eight maximum chlorophyll-specific carbon fixation rates within the water column (P_{opt}^b): M1-M8.

Due to the strong thermocline formation, the temperate regions experience significant seasonal variations in the stratification layer depth. In winter, this depth rises towards the surface in shallow (weak stratification) and moves downward towards the deep (strong stratification) in summer due to the weak thermocline condition. This suggests that nutrients are not a limiting factor for primary productivity, but it is mainly light-limited in winter. The spring is associated with strong vertical mixing of nutrients, availability of light and production variations similar to those observed in the polar region [64]. During summer, the temperate regions receive a high PAR which results in strong stratification (thermocline layer in shallower depth) and limits vertical mixing. This leads to the nutrient-depleted conditions and decreased productivity. In the beginning of the autumn, the temperature decreases, the thermocline becomes weaker, and the storm condition breaks the stratification, bringing up the nutrient-rich deep waters to the surface waters and producing autumn blooms (Fig. 10 (j) and (k)). However, the living

TABLE 5. Comparison of the DRPP models obtained from the P_{opt}^b (M1 – M8) and P_{rel}^b using the PAR_{rel} and ζ_z data. (UNIT: $mg\ C\ m^{-3}\ d^{-1}$).

MODEL	MRE (ABS)	PCC	MAE	RMSE	MNB
<i>DRPP obtained from the P_{rel}^b using PAR_{rel} - DRPP(PAR_{rel})</i>					
M1_PAR	1.846	0.735	22.023	45.476	-9.469
M2_PAR	1.507	0.734	19.586	39.944	-2.588
M3_PAR	1.644	0.261	23.934	55.666	13.787
M4_PAR	1.620	0.676	24.019	51.739	-7.043
M5_PAR	1.593	0.586	21.071	46.130	8.506
M6_PAR	1.454	0.706	18.713	39.860	3.847
M7_PAR	1.482	0.735	19.522	40.101	-2.409
M8_PAR	1.441	0.729	18.467	38.270	2.003
<i>DRPP obtained from the P_{rel}^b using ζ_z - DRPP(ζ_z)</i>					
M1_OD	1.407	0.752	20.018	41.054	-5.197
M2_OD	1.169	0.750	18.443	37.627	1.013
M3_OD	1.298	0.275	23.813	55.951	15.718
M4_OD	1.308	0.696	22.375	46.893	-3.017
M5_OD	1.274	0.605	20.918	46.186	10.976
M6_OD	1.140	0.721	18.336	39.838	6.789
M7_OD	1.162	0.752	18.422	37.643	1.175
M8_OD	1.137	0.746	17.960	37.710	5.134

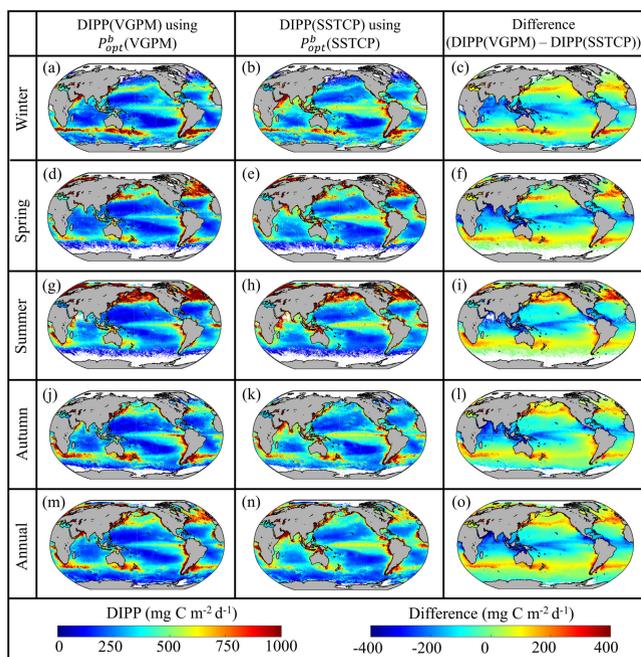


FIGURE 10. Comparison of the seasonal DIPP products derived from the VGPM model: M1 (P_{opt}^b (VGPM)) and tri-parameter model: M8 (P_{opt}^b (SSTCP)) along with their differences (DIPP(M1)-DIPP(M8)) for (a-c) winter, (d-f) spring, (g-i) summer, (j-l) autumn, and (m-o) annual of 2020.

period of autumn blooms is short. As the winter approaches, the temperate regions receive minimal light flux and hence low PP (mainly light-limited).

In tropical oceanic waters, the PAR is high at the sea surface throughout the year and causes the ocean surface warmer, highly stratified and strong thermocline conditions (nutrients limited). As a result, productivity is low for all

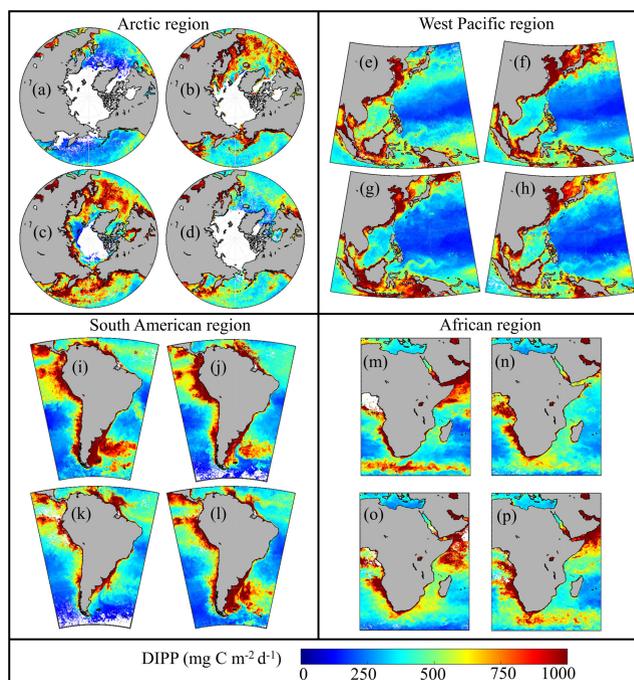


FIGURE 11. Comparison of the seasonal DIPP products of the tri-parameter models, M8 (P_{opt}^b (SSTCP)) for (a-d) Arctic, (e-h) West Pacific, (i-l) South American and (m-p) African regions for the season of winter, spring, summer and autumn of 2020 respectively.

seasons throughout the year (similar to the central ocean) (Fig. 10 (m) and (n)) [65].

Furthermore, we investigated the seasonal variation in DIPP(VGPM) and DIPP(SSTCP) derived from the regional MODIS-Aqua images for the Arctic, West Pacific, South America and Africa (Fig. 11). In northern hemisphere (Arctic region), the surface-reaching PAR and

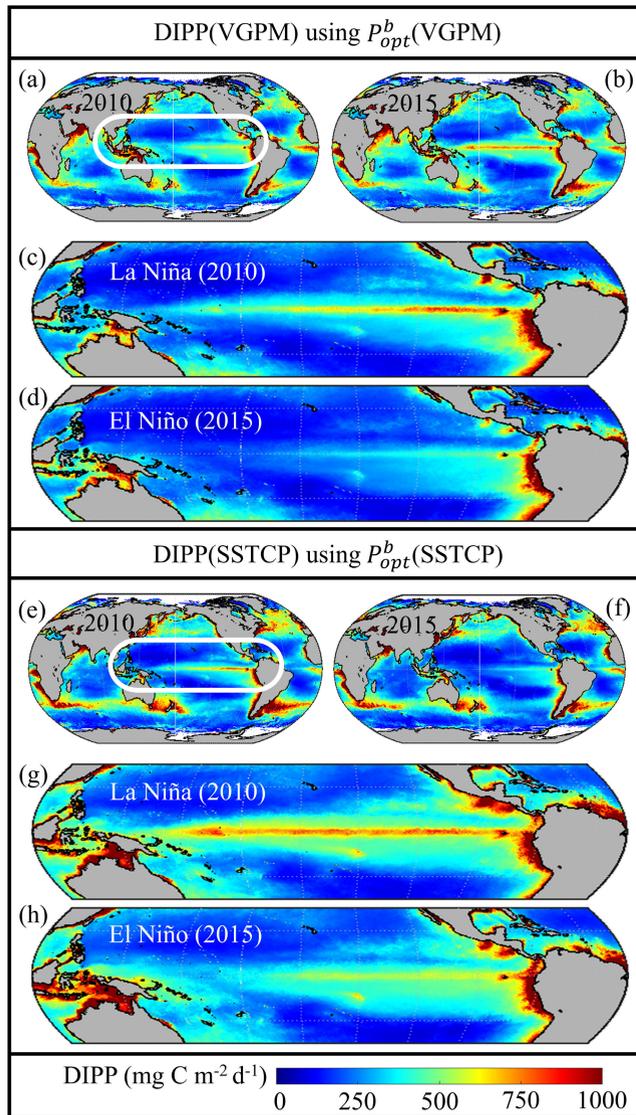


FIGURE 12. Comparison of the annual DIPP products derived from (a-d) VGPM model: M1 (P_{opt}^b (VGPM)) and (e-h) tri-parameter model: M8 (P_{opt}^b (SSTCP)) for the year of 2010 and 2015 respectively. The white colour bounded area is used to show the effects of the La Niña and El Niño events in the tropical waters.

chlorophyll concentrations are higher and resulting high PP (Fig. 11 (b) and (c)). In contrast, the southern hemisphere receives low surface PAR and chlorophyll concentration which consequently has a low rate of primary production (Fig. 11 (a) and (d)). In autumn and winter, the southern hemisphere receives high PAR and leads to increased chlorophyll concentration and primary productivity (Fig. 11 (i and l), and (m and p) respectively).

The El Niño and La Niña events can impact the spatiotemporal variability of DIPP by controlling the mixing of nutrients and phytoplankton growth in the global ocean. These events are more predominant to influence the changes in the weather patterns that weaken the eastern trade wind and cause temperature variation in the equatorial Pacific region [66]. To demonstrate these impacts and associated annual global

variation in DIPP (VGPM and SSTCP), the MODIS-Aqua data were processed for the year 2010 (strong La Niña) and 2015 (strong El Niño) and presented in Fig. 12 (a and b) and (e and f) respectively.

During El Niño, the unusual warming of surface waters drives the global climate patterns and changes the wind pattern, rainfall, and sea-surface temperature on the equator [67]. Especially in the equatorial Pacific region, chlorophyll concentration and productivity become low, which is due to the weak upwelling activity (Fig. 12 (d) and (h)) [68]. In La Niña, there was unusual cooling of surface waters (opposite process), strengthened upwelling, and mixing of nutrient-rich water from the bottom layer to the surface waters, and the increased chlorophyll concentration and high phytoplankton production in equatorial Pacific regions as shown in Fig. 12 (c) and (g) [69]. The ENSO is not only impacting the equatorial Pacific oceanic regimes but extending these effects to Eastern Indian and Indonesian oceanic waters, Gulf of Mexico and western Atlantic (subtropical) regions. Overall, the DIPP(VGPM) products yielded the lower PP values than the DIPP(SSTCP) in the equatorial region and slightly higher PP in the mid-latitudes during the El Niño and La Niña scenarios.

VII. SUMMARY AND CONCLUSION

The present work consisted of three major studies: i) Development and validation of DRPP model using the ζ_z and PAR_{rel} measurements, ii) Development of an efficient algorithm to estimate P_{opt}^b in diverse marine environment conditions, and iii) Demonstration of the DIPP products with the inputs of M1 and M8 models. To achieve the accurate global DRPP/DIPP, the input parameters (P_z^b , P_{opt}^b and P_{rel}^b) were modelled as the function of the important environmental forcing variables (biogeochemical and physiological parameters). In this study, the various combinations of SST, SCHL and SPAR were considered to develop the robust P_{opt}^b models (uni-, bi- and tri-parameter models). The statistical comparison results indicate that the tri-parameter model (M8) outperformed the other models (M1-M7). To describe the subsurface light field with the effects of light-limitation, saturation and photo-inhibition, two different models for estimating P_{rel}^b were also developed using PAR_{rel} and ζ_z data. Consequently, sixteen DRPP models were constructed with the inputs of P_{rel}^b and P_{opt}^b . Statistical results demonstrated that the DRPP(M8_OD) has a relatively better performance than the other models (DRPP(M1_OD-M7_OD) and DRPP(M1_PAR-M8_PAR)). To further evaluate these models, the global-scale (ocean basin) DIPP products were investigated using MODIS-Aqua data.

Finally, this study also demonstrated the spatial and temporal variations of P_{opt}^b and DIPP products for the year 2020. The regional DIPP images were produced to analyze the capability of the applied models. The statistical results indicate that the M8 based P_{opt}^b , DRPP and DIPP models are applicable to diverse marine environments. The global annual average of DIPP products was estimated around

200-400 mg C m⁻² d⁻¹, where the upwelling regions contributed to a higher PP. For example, the annual DIPP was 550-800 mg C m⁻² d⁻¹ off California coast and 900-1100 mg C m⁻² d⁻¹ off Peru and Benguela coasts. The central ocean produced a lesser annual DIPP (50-150 mg C m⁻² d⁻¹) than the other ocean regions. The Southern Ocean waters are associated with a higher level of nutrients and a lower level of light, resulting the diminished phytoplankton PP (250-550 mg C m⁻² d⁻¹). The new models with the appropriate physiological parameters (P_{opt}^b and P_{rel}^b) could significantly improve the accuracy of DRPP and DIPP products.

In this study, SST was used as a proxy to account for nutrients in global ocean waters. A better representation of macro/micro-nutrients is further required to capture more accurate seasonal patterns in PP due to the phytoplankton community composition. Though the present models improved the PP estimates in the tropical and temperate regions, there could be uncertainties in the polar region due to the freshwater runoff from melting of icesheets and glaciers. Low light and nutrients, low solar angle and high cloudiness can significantly impact the upper ocean stratification and related processes. In such regions, accurate estimates of PP can be obtained through further refinements by using i) vertical PAR profiles which are defined as a function of the SPAR and SCHL, ii) vertical chlorophyll profiles which are defined as a function of the SCHL, and iii) other governing parameters such as size-fractionated phytoplankton, upwelling wind stress, and mixed layer depth in the model formulation. In conclusion, the improved and optimized models as presented in this study can be used with the water colour remote sensing sensors to elucidate changes in phytoplankton biomass, assimilation efficiency, and seasonal and inter-annual variations of DIPP at regional and global scales.

ACKNOWLEDGMENT

The authors would like to thank the Ocean Biology Processing Group of NASA for the distribution of MODIS-Aqua data, also would like to thank all the data providers and their teams for collecting, processing, and archiving the data for research purposes, also would like to thank the Oregon State University Primary Productivity (OSPP) and Biological and Chemical Oceanography-Data Management Office Primary Productivity (BCO-DMOPP) teams for making the in-situ data available to the research community, also would like to thank the primary productivity projects' principal investigators (PIs): Behrenfeld and Falkowski (Rutgers University), Babin and Morel (Laboratoire de Physique et Chimie Marines), O'Reilly (NOAA, NFMS, Narragansett Laboratory), Balch (Bigelow Laboratory for Ocean Sciences), Barber (Duke University), Bender (University of Rhode Island, URI-GSO), Eppley and Marra (Lamont-Doherty Earth Observatory), Dickey (University of Southern California), and Gardner (Texas A&M University), and also would like to thank the two reviewers for their constructive comments and suggestions on the original manuscript.

REFERENCES

- [1] C. B. Field, M. J. Behrenfeld, J. T. Randerson, and P. Falkowski, "Primary production of the biosphere: Integrating terrestrial and oceanic components," *Science*, vol. 281, no. 5374, pp. 237-240, Jul. 1998, doi: [10.1126/science.281.5374.237](https://doi.org/10.1126/science.281.5374.237).
- [2] P. G. Falkowski and J. A. Raven, *Aquatic Photosynthesis*. Princeton, NJ, USA: Princeton Univ. Press, 2013.
- [3] R. J. Geider et al., "Primary productivity of planet earth: Biological determinants and physical constraints in terrestrial and aquatic habitats," *Global Change Biol.*, vol. 7, no. 8, pp. 849-882, Dec. 2001, doi: [10.1046/j.1365-2486.2001.00448.x](https://doi.org/10.1046/j.1365-2486.2001.00448.x).
- [4] T. Parsons, M. Takahashi, and B. Hargrave, *Biological Oceanographic Processes*, 3rd ed. Oxford, U.K.: Pergamon Press, 1984.
- [5] J. J. Middelburg, "Primary production: From inorganic to organic carbon," in *Marine Carbon Biogeochemistry: A Primer for Earth System Scientists*. Cham, Switzerland: Springer, 2019, pp. 9-35, doi: [10.1007/978-3-030-10822-9_2](https://doi.org/10.1007/978-3-030-10822-9_2).
- [6] J. J. Cullen, "Primary production methods," in *Encyclopedia of Ocean Sciences*. Amsterdam, The Netherlands: Elsevier, 2001, pp. 578-584, doi: [10.1016/B978-012374473-9.00203-4](https://doi.org/10.1016/B978-012374473-9.00203-4).
- [7] D. M. Sigman and M. P. Hain, "The biological productivity of the ocean," *Nature Educ. Knowl.*, vol. 3, no. 10, p. 21, 2012.
- [8] R. W. Eppley, "Estimating phytoplankton growth rates in the central oligotrophic oceans," in *Primary Productivity in the Sea*. Boston, MA, USA: Springer, 1980, pp. 231-242, doi: [10.1007/978-1-4684-3890-1_13](https://doi.org/10.1007/978-1-4684-3890-1_13).
- [9] G. Slawyk, Y. Collos, and J.-C. Auclair, "The use of the ¹³C and ¹⁵N isotopes for the simultaneous measurement of carbon and nitrogen turnover rates in marine phytoplankton," *Limnol. Oceanogr.*, vol. 22, no. 5, pp. 925-932, Sep. 1977, doi: [10.4319/lo.1977.22.5.0925](https://doi.org/10.4319/lo.1977.22.5.0925).
- [10] E. S. Nielsen, "The use of radio-active carbon (¹⁴C) for measuring organic production in the sea," *ICES J. Mar. Sci.*, vol. 18, no. 2, pp. 117-140, Aug. 1952, doi: [10.1093/icesjms/18.2.117](https://doi.org/10.1093/icesjms/18.2.117).
- [11] R. C. Dugdale and J. J. Goering, "Uptake of new and regenerated forms of nitrogen in primary productivity," *Limnol. Oceanogr.*, vol. 12, no. 2, pp. 196-206, Apr. 1967, doi: [10.4319/lo.1967.12.2.0196](https://doi.org/10.4319/lo.1967.12.2.0196).
- [12] P. J. I. Williams and J. E. Robertson, "Overall planktonic oxygen and carbon dioxide metabolisms: The problem of reconciling observations and calculations of photosynthetic quotients," *J. Plankton Res.*, vol. 13, no. suppl, pp. 153-169, Jan. 1991, doi: [10.1093/oxfordjournals.plankt.a042366](https://doi.org/10.1093/oxfordjournals.plankt.a042366).
- [13] P. J. le B. Williams, P. J. Morris, and D. M. Karl, "Net community production and metabolic balance at the oligotrophic ocean site, station ALOHA," *Deep Sea Res. I: Oceanograph. Res. Papers*, vol. 51, no. 11, pp. 1563-1578, Nov. 2004, doi: [10.1016/j.dsr.2004.07.001](https://doi.org/10.1016/j.dsr.2004.07.001).
- [14] Z. Kolber and P. G. Falkowski, "Use of active fluorescence to estimate phytoplankton photosynthesis in situ," *Limnol. Oceanogr.*, vol. 38, no. 8, pp. 1646-1665, Dec. 1993, doi: [10.4319/lo.1993.38.8.1646](https://doi.org/10.4319/lo.1993.38.8.1646).
- [15] Z. S. Kolber, O. Prášil, and P. G. Falkowski, "Measurements of variable chlorophyll fluorescence using fast repetition rate techniques: Defining methodology and experimental protocols," *Biochimica Biophysica Acta (BBA)-Bioenergetics*, vol. 1367, nos. 1-3, pp. 88-106, Oct. 1998, doi: [10.1016/S0005-2728\(98\)00135-2](https://doi.org/10.1016/S0005-2728(98)00135-2).
- [16] T. Hama, T. Miyazaki, Y. Ogawa, T. Iwakuma, M. Takahashi, A. Otsuki, and S. Ichimura, "Measurement of photosynthetic production of a marine phytoplankton population using a stable ¹³C isotope," *Mar. Biol.*, vol. 73, no. 1, pp. 31-36, 1983, doi: [10.1007/BF00396282](https://doi.org/10.1007/BF00396282).
- [17] H. A. Bouman, T. Platt, M. Doblin, F. G. Figueiras, K. Gudmundsson, H. G. Gudfinnsson, B. Huang, A. Hickman, M. Hiscock, T. Jackson, V. A. Lutz, F. Mélin, F. Rey, P. Pepin, V. Segura, G. H. Tilstone, V. van Dongen-Vogels, and S. Sathyendranath, "Photosynthesis-irradiance parameters of marine phytoplankton: Synthesis of a global data set," *Earth Syst. Sci. Data*, vol. 10, no. 1, pp. 251-266, Feb. 2018, doi: [10.5194/essd-10-251-2018](https://doi.org/10.5194/essd-10-251-2018).
- [18] M.-E. Carr et al., "A comparison of global estimates of marine primary production from ocean color," *Deep Sea Res. II, Top. Stud. Oceanogr.*, vol. 53, nos. 5-7, pp. 741-770, Mar. 2006, doi: [10.1016/j.dsr2.2006.01.028](https://doi.org/10.1016/j.dsr2.2006.01.028).
- [19] D. Antoine, A. Morel, and J.-M. André, "Algal pigment distribution and primary production in the eastern Mediterranean as derived from coastal zone color scanner observations," *J. Geophys. Res.*, vol. 100, no. C8, p. 16193, 1995, doi: [10.1029/95JC00466](https://doi.org/10.1029/95JC00466).
- [20] D. Antoine, J.-M. André, and A. Morel, "Oceanic primary production: 2. Estimation at global scale from satellite (coastal zone color scanner) chlorophyll," *Global Biogeochem. Cycles*, vol. 10, no. 1, pp. 57-69, Mar. 1996, doi: [10.1029/95GB02832](https://doi.org/10.1029/95GB02832).

- [21] International Ocean-Colour Coordinating Group. (2022). *Historical Ocean-Colour Sensors*. Accessed: Sep. 21, 2022. [Online]. Available: <https://ioccg.org/resources/missions-instruments/historical-ocean-colour-sensors/>
- [22] International Ocean-Colour Coordinating Group. (2022). *Current Ocean-Colour Sensors*. Accessed: Sep. 21, 2022. [Online]. Available: <https://ioccg.org/resources/missions-instruments/current-ocean-colour-sensors/>
- [23] *Reports of the International Ocean-Colour Coordinating Group Remote Sensing of Inherent Optical Properties: Fundamentals, Tests of Algorithms, and Applications*, IOCCG, Dartmouth, NS, Canada, 2006.
- [24] T. Platt and S. Sathyendranath, "Estimators of primary production for interpretation of remotely sensed data on ocean color," *J. Geophys. Res., Oceans*, vol. 98, no. C8, pp. 14561–14576, 1993.
- [25] D. Antoine and A. Morel, "Oceanic primary production: I. Adaptation of a spectral light-photosynthesis model in view of application to satellite chlorophyll observations," *Global Biogeochem. Cycles*, vol. 10, no. 1, pp. 43–55, Mar. 1996, doi: [10.1029/95GB02831](https://doi.org/10.1029/95GB02831).
- [26] M. E. Ondrusek, R. R. Bidigare, K. Waters, and D. M. Karl, "A predictive model for estimating rates of primary production in the subtropical North Pacific Ocean," *Deep Sea Res. II, Topical Stud. Oceanogr.*, vol. 48, nos. 8–9, pp. 1837–1863, Jan. 2001, doi: [10.1016/S0967-0645\(00\)00163-6](https://doi.org/10.1016/S0967-0645(00)00163-6).
- [27] J. Campbell et al., "Comparison of algorithms for estimating ocean primary production from surface chlorophyll, temperature, and irradiance," *Global Biogeochem. Cycles*, vol. 16, no. 3, pp. 9–19–15, Sep. 2002, doi: [10.1029/2001GB001444](https://doi.org/10.1029/2001GB001444).
- [28] M. J. Behrenfeld, E. Boss, D. A. Siegel, and D. M. Shea, "Carbon-based ocean productivity and phytoplankton physiology from space," *Global Biogeochem. Cycles*, vol. 19, no. 1, pp. 1–14, Mar. 2005, doi: [10.1029/2004GB002299](https://doi.org/10.1029/2004GB002299).
- [29] T. Westberry, M. J. Behrenfeld, D. A. Siegel, and E. Boss, "Carbon-based primary productivity modeling with vertically resolved photoacclimation," *Global Biogeochem. Cycles*, vol. 22, no. 2, pp. 1–18, Jun. 2008, doi: [10.1029/2007GB003078](https://doi.org/10.1029/2007GB003078).
- [30] T. Platt, S. Sathyendranath, M.-H. Forget, G. N. White, C. Caverhill, H. Bouman, E. Devred, and S. Son, "Operational estimation of primary production at large geographical scales," *Remote Sens. Environ.*, vol. 112, no. 8, pp. 3437–3448, Aug. 2008, doi: [10.1016/j.rse.2007.11.018](https://doi.org/10.1016/j.rse.2007.11.018).
- [31] M. J. Behrenfeld and P. G. Falkowski, "A consumer's guide to phytoplankton primary productivity models," *Limnol. Oceanogr.*, vol. 42, no. 7, pp. 1479–1491, Nov. 1997, doi: [10.4319/lo.1997.42.7.1479](https://doi.org/10.4319/lo.1997.42.7.1479).
- [32] Z. Lee, J. Marra, M. J. Perry, and M. Kahru, "Estimating oceanic primary productivity from ocean color remote sensing: A strategic assessment," *J. Mar. Syst.*, vol. 149, pp. 50–59, Sep. 2015, doi: [10.1016/j.jmarsys.2014.11.015](https://doi.org/10.1016/j.jmarsys.2014.11.015).
- [33] W. Li, S. P. Tiwari, H. M. El-Askary, M. A. Qurban, V. Amiridis, K. P. ManiKandan, M. J. Garay, O. V. Kalashnikova, T. C. Piechota, and D. C. Struppa, "Synergistic use of remote sensing and modeling for estimating net primary productivity in the Red Sea with VGPM, Eppley-VGPM, and CbPM models intercomparison," *IEEE Trans. Geosci. Remote Sens.*, vol. 58, no. 12, pp. 8717–8734, Dec. 2020, doi: [10.1109/TGRS.2020.2990373](https://doi.org/10.1109/TGRS.2020.2990373).
- [34] IOCCG. (2012). *IOCCG Report Number 12: Ocean-Colour Observations From a Geostationary Orbit*. [Online]. Available: http://www.ioccg.org/reports/IOCCG_Report_12.pdf
- [35] *IOCCG Report Number 19, 2020 Synergy Between Ocean Colour and Biogeochemical/Ecosystem Models*, IOCCG, Dartmouth, NS, Canada, 2016.
- [36] R. Gupta, L. K. Sharma, S. K. Patidar, A. Raj, and R. Naik, "Potential of remote sensing for improved understanding of aquatic chlorophyll, biomass and primary productivity estimation," *LS- Int. J. Life Sci.*, vol. 11, no. 1, pp. 61–75, 2022, doi: [10.5958/2319-1198.2022.00006.9](https://doi.org/10.5958/2319-1198.2022.00006.9).
- [37] T. Soomets, T. Kutser, A. Wüest, and D. Buffard, "Spatial and temporal changes of primary production in a deep peri-alpine lake," *Inland Waters*, vol. 9, no. 1, pp. 49–60, Jan. 2019, doi: [10.1080/20442041.2018.1530529](https://doi.org/10.1080/20442041.2018.1530529).
- [38] M. A. M. Friedrichs et al., "Assessing the uncertainties of model estimates of primary productivity in the tropical Pacific Ocean," *J. Mar. Syst.*, vol. 76, nos. 1–2, pp. 113–133, 2009, doi: [10.1016/j.jmarsys.2008.05.010](https://doi.org/10.1016/j.jmarsys.2008.05.010).
- [39] S. Tang, C. Chen, H. Zhan, and T. Zhang, "Determination of ocean primary productivity using support vector machines," *Int. J. Remote Sens.*, vol. 29, no. 21, pp. 6227–6236, Nov. 2008, doi: [10.1080/01431160802175355](https://doi.org/10.1080/01431160802175355).
- [40] G. Kulk et al., "Primary production, an index of climate change in the ocean: Satellite-based estimates over two decades," *Remote Sens.*, vol. 12, no. 5, p. 826, Mar. 2020, doi: [10.3390/rs12050826](https://doi.org/10.3390/rs12050826).
- [41] P. G. Falkowski, R. T. Barber, and V. Smetacek, "Biogeochemical controls and feedbacks on ocean primary production," *Science*, vol. 281, no. 5374, pp. 200–206, Jul. 1998, doi: [10.1126/science.281.5374.200](https://doi.org/10.1126/science.281.5374.200).
- [42] M. J. Behrenfeld and P. G. Falkowski, "Photosynthetic rates derived from satellite-based chlorophyll concentration," *Limnol. Oceanogr.*, vol. 42, no. 1, pp. 1–20, 1997, doi: [10.4319/lo.1997.42.1.0001](https://doi.org/10.4319/lo.1997.42.1.0001).
- [43] P. G. Falkowski, *Satellite Primary Productivity Data and Algorithm Development: A Science Plan for Mission to Planet Earth*. Washington, DC, USA: NASA, 1998.
- [44] A. Morel, "Light and marine photosynthesis: A spectral model with geochemical and climatological implications," *Prog. Oceanogr.*, vol. 26, no. 3, pp. 263–306, Jan. 1991, doi: [10.1016/0079-6611\(91\)90004-6](https://doi.org/10.1016/0079-6611(91)90004-6).
- [45] I. Asanuma, "Depth and time resolved primary productivity model examined for optical properties of water," in *Global Climate Change and Response of Carbon Cycle in the Equatorial Pacific and Indian Oceans and Adjacent Landmasses* (Elsevier Oceanography Series), vol. 73. Amsterdam, The Netherlands: Elsevier, 2007, ch. 4, pp. 89–106, doi: [10.1016/S0422-9894\(06\)73004-5](https://doi.org/10.1016/S0422-9894(06)73004-5).
- [46] J. A. Schullien, M. J. Behrenfeld, J. W. Hair, C. A. Hostetler, and M. S. Twardowski, "Vertically-resolved phytoplankton carbon and net primary production from a high spectral resolution lidar," *Opt. Exp.*, vol. 25, no. 12, p. 13577, Jun. 2017, doi: [10.1364/OE.25.013577](https://doi.org/10.1364/OE.25.013577).
- [47] S. Bailey. (2023). *MODIS/Aqua Ocean Color Reprocessing 2022.0*. OceanColor Webmaster. Accessed: Jan. 9, 2023. [Online]. Available: <https://oceancolor.gsfc.nasa.gov/reprocessing/r2022/aqua/>
- [48] S. Bailey. (2023). *Long-Wave Sea Surface Temperature (SST)*. OceanColor Webmaster. Accessed: Jan. 9, 2023. [Online]. Available: https://oceancolor.gsfc.nasa.gov/atbd/sst/#sec_4
- [49] A. B. Demidov, S. A. Mosharov, V. A. Artyemyev, A. N. Stupnikova, U. V. Simakova, and S. V. Vazyulya, "Depth-integrated and depth-resolved models of Kara Sea primary production," *Oceanology*, vol. 56, no. 4, pp. 515–526, Jul. 2016, doi: [10.1134/S0001437016040020](https://doi.org/10.1134/S0001437016040020).
- [50] A. Morel and J. Berthon, "Surface pigments, algal biomass profiles, and potential production of the euphotic layer: Relationships reinvestigated in view of remote-sensing applications," *Limnol. Oceanogr.*, vol. 34, no. 8, pp. 1545–1562, Dec. 1989, doi: [10.4319/lo.1989.34.8.1545](https://doi.org/10.4319/lo.1989.34.8.1545).
- [51] M. J. Behrenfeld, W. E. Esaias, and K. R. Turpie, "Assessment of primary production at the global scale," in *Phytoplankton Productivity*. Oxford, U.K.: Blackwell, 2002, pp. 156–186, doi: [10.1002/9780470995204.ch7](https://doi.org/10.1002/9780470995204.ch7).
- [52] T. Wiens. (2022). *Day Length*. MATLAB Central File Exchange. The MathWorks, Inc. Accessed: Feb. 1, 2022. [Online]. Available: <https://in.mathworks.com/matlabcentral/fileexchange/20390-day-length>
- [53] A. Longhurst, S. Sathyendranath, T. Platt, and C. Caverhill, "An estimate of global primary production in the ocean from satellite radiometer data," *J. Plankton Res.*, vol. 17, no. 6, pp. 1245–1271, 1995, doi: [10.1093/plankt/17.6.1245](https://doi.org/10.1093/plankt/17.6.1245).
- [54] T. Platt, C. Caverhill, and S. Sathyendranath, "Basin-scale estimates of oceanic primary production by remote sensing: The North Atlantic," *J. Geophys. Res., Oceans*, vol. 96, no. C8, p. 15147, 1991, doi: [10.1029/91JC01118](https://doi.org/10.1029/91JC01118).
- [55] T. Platt and S. Sathyendranath, "Oceanic primary production: Estimation by remote sensing at local and regional scales," *Science*, vol. 241, no. 4873, pp. 1613–1620, Sep. 1988, doi: [10.1126/science.241.4873.1613](https://doi.org/10.1126/science.241.4873.1613).
- [56] S. Milutinović and L. Bertino, "Assessment and propagation of uncertainties in input terms through an ocean-color-based model of primary productivity," *Remote Sens. Environ.*, vol. 115, no. 8, pp. 1906–1917, Aug. 2011, doi: [10.1016/j.rse.2011.03.013](https://doi.org/10.1016/j.rse.2011.03.013).
- [57] M. Gómez-Letona, A. G. Ramos, J. Coca, and J. Arístegui, "Trends in primary production in the Canary current upwelling system—A regional perspective comparing remote sensing models," *Frontiers Mar. Sci.*, vol. 4, pp. 1–18, Nov. 2017, doi: [10.3389/fmars.2017.00370](https://doi.org/10.3389/fmars.2017.00370).
- [58] R. Sauzède, H. C. Bittig, H. Claustre, O. Pasqueron de Fommervault, J.-P. Gattuso, L. Legendre, and K. S. Johnson, "Estimates of water-column nutrient concentrations and carbonate system parameters in the global ocean: A novel approach based on neural networks," *Frontiers Mar. Sci.*, vol. 4, pp. 1–17, May 2017, doi: [10.3389/fmars.2017.00128](https://doi.org/10.3389/fmars.2017.00128).
- [59] H. C. Bittig, T. Steinhoff, H. Claustre, B. Fiedler, N. L. Williams, R. Sauzède, A. Körtzinger, and J.-P. Gattuso, "An alternative to static climatologies: Robust estimation of open ocean CO₂ variables and nutrient concentrations from T, S, and O₂ data using Bayesian neural networks," *Frontiers Mar. Sci.*, vol. 5, pp. 1–29, Sep. 2018, doi: [10.3389/fmars.2018.00328](https://doi.org/10.3389/fmars.2018.00328).
- [60] T. Kameda and J. Ishizaka, "Size-fractionated primary production estimated by a two-phytoplankton community model applicable to ocean color remote sensing," *J. Oceanogr.*, vol. 61, no. 4, pp. 663–672, Aug. 2005, doi: [10.1007/s10872-005-0074-7](https://doi.org/10.1007/s10872-005-0074-7).

- [61] H. K. K. Sundararaman, P. Shanmugam, and P. V. Nagamani, "Robust extension of the simple sea-surface irradiance model to handle cloudy conditions for the global ocean using satellite remote sensing data," *Adv. Space Res.*, vol. 71, no. 3, pp. 1486–1509, Feb. 2023, doi: [10.1016/j.asr.2022.10.009](https://doi.org/10.1016/j.asr.2022.10.009).
- [62] T. C. Peterson and M. O. Baringer, "State of the climate in 2008," *Bull. Amer. Meteorolog. Soc.*, vol. 90, no. 8, pp. S1–S196, Aug. 2009, doi: [10.1175/BAMS-90-8-StateoftheClimate](https://doi.org/10.1175/BAMS-90-8-StateoftheClimate).
- [63] S. Gaines and A. Satie. (2017). *Background: Upwelling*. NOAA Ocean Explorer Website: Sanctuary Quest. Accessed: Sep. 25, 2022. [Online]. Available: <https://oceanexplorer.noaa.gov/explorations/02quest/background/upwelling/upwelling.html>
- [64] M. J. Behrenfeld, "Abandoning Sverdrup's critical depth hypothesis on phytoplankton blooms," *Ecology*, vol. 91, no. 4, pp. 977–989, Apr. 2010, doi: [10.1890/09-1207.1](https://doi.org/10.1890/09-1207.1).
- [65] M. J. Behrenfeld, R. T. O'Malley, D. A. Siegel, C. R. McClain, J. L. Sarmiento, G. C. Feldman, A. J. Milligan, P. G. Falkowski, R. M. Letelier, and E. S. Boss, "Climate-driven trends in contemporary ocean productivity," *Nature*, vol. 444, no. 7120, pp. 752–755, 2006, doi: [10.1038/nature05317](https://doi.org/10.1038/nature05317).
- [66] G. Feldman, D. Clark, and D. Halpern, "Satellite color observations of the phytoplankton distribution in the eastern equatorial Pacific during the 1982–1983. El Niño," *Science*, vol. 226, no. 4678, pp. 1069–1071, Nov. 1984, doi: [10.1126/science.226.4678.1069](https://doi.org/10.1126/science.226.4678.1069).
- [67] J. I. Goes, P. G. Thoppil, H. D. R. Gomes, and J. T. Fasullo, "Warming of the Eurasian landmass is making the Arabian sea more productive," *Science*, vol. 308, no. 5721, pp. 545–547, Apr. 2005, doi: [10.1126/science.1106610](https://doi.org/10.1126/science.1106610).
- [68] F. P. Chavez, J. T. Pennington, C. G. Castro, J. P. Ryan, R. P. Michisaki, B. Schlining, P. Walz, K. R. Buck, A. McFadyen, and C. A. Collins, "Biological and chemical consequences of the 1997–1998 El Niño in central California waters," *Prog. Oceanogr.*, vol. 54, nos. 1–4, pp. 205–232, Jul. 2002, doi: [10.1016/S0079-6611\(02\)00050-2](https://doi.org/10.1016/S0079-6611(02)00050-2).
- [69] J. A. Yoder and M. A. Kennelly, "Seasonal and ENSO variability in global ocean phytoplankton chlorophyll derived from 4 years of SeaWiFS measurements," *Global Biogeochem. Cycles*, vol. 17, no. 4, pp. 1–14, Dec. 2003, doi: [10.1029/2002GB001942](https://doi.org/10.1029/2002GB001942).



Harish Kumar Kashtan Sundararaman received the B.E. degree in civil engineering from the SACS MAVMM Engineering College (Madurai), Anna University, Chennai, Tamil Nadu, India, in 2015, and the M.E. degree in remote sensing and geomatics from the College of Engineering-Guindy, Anna University, in 2017. He has been a Ph.D. Scholar with the Department of Ocean Engineering, IIT Madras, Chennai. His research interest includes developing algorithms to retrieve level-2 products from satellite image.



Palanisamy Shanmugam received the Ph.D. degree in optical/microwave remote sensing techniques from Anna University, Chennai, India, in 2002. He is currently a Professor/a National Geospatial Chair Professor with the Department of Ocean Engineering, IIT Madras, Chennai. He has been a principal investigator of several projects funded by the Government of India. His research interests include ocean optics and imaging, satellite oceanography, radiative transfer in the ocean, algorithm/model development, and underwater wireless optical communication.

• • •